

IMPACT OF THE COOLING RATE ON FOG FORMATION

Arun Gandhi ⁽¹⁾, István Geresdi ⁽²⁾ , András Peterka ⁽²⁾,
András Zénó Gyöngyösi ^(1,3), Ágoston Vilmos Tordai ⁽¹⁾ , Péter Torma ^(4,5) ,
András Rehák ⁽⁶⁾, Mariann Bíró-Szilágyi ⁽⁶⁾, Gyula Horváth ⁽⁷⁾,
Zita Ferenczi ⁽⁷⁾ , Kornélia Imre ⁽⁸⁾, István Lázár ⁽⁹⁾, Tamás Weidinger ⁽¹⁾ 

⁽¹⁾ ELTE Eötvös Loránd University, Institute of Geography and Earth Sciences,
Department of Meteorology, H-1117 Budapest, Pázmány P. st. 1/A, Hungary

⁽²⁾ Institute of Geography and Earth Sciences, Faculty of Sciences,
University of Pécs, Ifjúság str. 6, 7624, Pécs, Hungary

⁽³⁾ Institute of Chemistry, Eötvös Loránd University, H-1518 Budapest, P.O. Box 32, Hungary

⁽⁴⁾ ELKH-SZTE Research Group for Photoacoustic Monitoring of Environmental Processes,
H-6701 Szeged, P.O. Box. 406, Hungary

⁽⁵⁾ National Laboratory for Water Science and Water Security,
Budapest University of Technology and Economics, Faculty of Civil Engineering,
Department of Hydraulic and Water Resources Engineering,
3 Műegyetem rkp., K building ground floor 12., H-1111 Budapest, Hungary

⁽⁶⁾ Department of Hydraulic and Water Resources Engineering,
Budapest University of Technology and Economics, 3 Műegyetem rkp.,
K building ground floor 12., H-1111 Budapest, Hungary

⁽⁷⁾ Hungarian Meteorological Service, Budapest, Kitaibel P. str. 1, H-1024 Budapest, Hungary

⁽⁸⁾ University of Pannonia, ELKH-PE Air Chemistry Research Group,
8201 Veszprém, P.O. Box 158, Hungary

⁽⁹⁾ Department of Meteorology, University of Debrecen,

H-4032 Debrecen Egyetem square 1., P.O. Box 13, Hungary

e-mail: arun.elte@gmail.com, geresdi@ttk.pte.hu, andras.zeno.gyongyosi@ttk.elte.hu,
tordai@student.elte.hu, torma.peter@epito.bme.hu, rehak.andras@epito.bme.hu,
szilagyi.mariann@epito.bme.hu, horvath.gy@met.hu, ferenczi.z@met.hu,
kornelia@almos.uni-pannon.hu, lazar.istvan@science.unideb.hu, weidi@staff.elte.hu

Introduction

Decrease of air temperature along with high specific humidity 2–3 hours before the fog onset is important factor in fog formation and evolution. Fog development is an interaction among the radiative cooling leading to saturation from the ground to the top of fog layer, and turbulent diffusion of water vapor causing dew formation (Duynderke, 1999). The moisture deposited on the surface results in release of latent heat causing further cooling near the surface. The magnitude of cooling rate is a key factor for aerosol activation process and influences the drop number concentration and their size distribution (Rangognio et al., 2009; Haeffelin et al., 2010).

Weak turbulent mixing promotes the fog formation. After the increase of shortwave radiation and/or wind speed, dissipation of fog can happen within from few minutes to hours. Several experiments have been conducted in the past to study the physical processes determine the fog formation, and most of these experiments focused on the impact of radiative cooling. The earliest papers published results about the radiative flux divergence near the surface (by Rider & Robinson, 1951; Funk, 1960; and Elliot, 1964). These studies asserted that the cooling rate near the surface is about 1 K hr^{-1} (or 1 °C hr^{-1}). Mason (1982) summarized the physical processes affecting the lifecycle of the fog. He concluded that outgoing long wave radiation from the surface results in radiative cooling of about 1 °C hr^{-1} . Duynderke (1999) evaluated the cooling rate, and found that it was about 3.5 K hr^{-1} at 1 m above the ground, and it was about

0.2–0.5 °C hr⁻¹ above the boundary layer. He asserted that cooling rate near to the surface was balanced by heating due to turbulence and inside the boundary layer, turbulence was dominant factor causing cooling.

Cooling rate has its maximum at the top of fog, and thus maximum amount of liquid water was condensed there (Rangognio et al., 2009). Rangognio et al. (2009) also found that the number concentration of activated aerosol particles depends on the cooling rates, and thus its value was different closed to the ground than at the top of fog. The authors observed a cooling rate of 4 °C hr⁻¹ near the surface, while cooling rates varied between 4 °C hr⁻¹ and 15 °C hr⁻¹ at the top of fog. Price (2011) asserted that the cooling rates during a radiation fog event varied between 1 and 4 °C hr⁻¹ three hours before the onset of fog and one hour into fog. Haeffelin et al. (2013) assessed that the cooling rate greater than 1 °C hr⁻¹ mitigated the fog formation, and rather promoted dew formation on the surface. Therefore, evaluation of a threshold value for cooling rate is essential because if the cooling rate is too large, the fog will dissipate efficiently due to the fast sedimentation of the droplets (Haeffelin et al., 2013; Dupont et al., 2016).

A micrometeorological fog experiment was performed at the main observatory of the Hungarian Meteorological Service (HMS) in Budapest (station ID 12843) from October to April 2020–21. This field campaign was designed to include simultaneous measurements of standard meteorological variables, radiative balance, vertical profiles of wind, temperature and humidity up to a height of 30 m. Furthermore, turbulent momentum, sensible and latent heat fluxes were evaluated, and concentration of the pollutants, both gases and aerosol particles were observed to study the environmental conditions under which fog develops, persists and dissipates (Weidinger et al., 2021). The main objective of the experiment is to construct a comprehensive database to study the characteristics and variability of fog events in order to improve our understanding of physiochemical, dynamical and other environmental factors, which influence the fog lifecycle.

In this study the time series of temperature with time resolution of 10 s and 10 Hz, before the onset of a fog, was studied. It has been utilized to find the breakpoints in the time series, and then perform linear regression analysis to calculate the cooling rate for the corresponding time periods.

Budapest Field Campaign

The experiment was performed during the winter half-year of 2020–21 (from 1st October to 31st March). Surface energy budget measurements started in the middle of November, and the measurements on a 30-m tower (temperature, relative humidity and wind speed profiles and Gill Sonic anemometer measurement at 30 m height) began at the end of December. The measuring site was the main observatory of the HMS located at 47.4292 N° and 19.1818 E° in Pestszentlőrinc, Budapest (station ID 12843) (Weidinger et al., 2021).

The main elements of the instrumentation implemented on the 30-m tower (*Figure 1*) are as follows: (i) Vaisala HMP-45C (temperature/relative humidity sensors) and Vaisala WA15 anemometer (wind speed detection) were installed at the heights of 9 m and 23 m. (ii) Gill sonic Windmaster 3D anemometer placed on top of the tower at the height of 30 m. The instruments installed on the tower are also listed in *Table 1*. *Figure 1* shows the picture of 30 m tower with instrumentations used to observed data to reconstruct the vertical profiles of the different physical variables. Eddy covariance system, installed at 5 m on small towers in about a distance of 20 m from the 30-m tower, was used to provide the components of the energy budget (Weidinger et al., 2021).

In this study the data about temperature observed at heights at 9 m, 23 m, and sonic temperature observed by Gill Sonic Anemometer are analyzed for better understanding the cooling rate impacts on the onset of foggy events.



Figure 1: 30-m meteorological tower for temperature and wind profile measurements along with eddy covariance measurements done at the top (30 m) using Gill sonic Windmaster 3D anemometer.

Table 1: Instrumentation of the 30-m meteorological tower.

Instrument	Height	Variables	Resolution
Gill sonic Windmaster 3D anemometer	30 m	u, v, w [m s^{-1}], T_s [$^{\circ}\text{C}$], turbulent fluxes (momentum and sensible heat): τ [$\text{kg m}^{-1}\text{s}^{-2}$], H [W m^{-2}]	10 Hz
Vaisala HMP-45C	23 m	T [$^{\circ}\text{C}$], Rh [%]	10 s
Vaisala WA15 anemometer	23 m	wind speed (V [m s^{-1}])	10 s
Vaisala HMP-45C	9 m	T [$^{\circ}\text{C}$], Rh [%]	10 s
Vaisala WA15 anemometer	9 m	wind speed (V [m s^{-1}])	10 s

Relationship between cooling rate and fog formation

The cooling of the surface layer along with high relative humidity are an important precursor to the formation of fog. The surface layer should cool down to allow the condensation of vapor on water soluble aerosol particles.

In this study the cooling rate ($\frac{\partial T}{\partial t}$) detected prior to the foggy event occurred on 24th November (03:30 – 22:30 UTC) in 2020 is analysed. This radiation type fog (based on the methodology of Tardif & Rasmussen (2007) and Lin et al. (2022)) formed due to radiative cooling of the ground. The knowledge of cooling rate is important for accurate evaluation of the rate of saturation.

A couple of hours before the onset of fog the change of saturation vapor pressure (e_s) with respect to temperature (T) is used for the calculation of rate of change of supersaturation (s). The supersaturation is the ratio of vapor pressure (e_a), which depends on the vapor content and saturation vapor pressure ($e_s(T)$). The partial time derivative of supersaturation ($s = \frac{e_a}{e_s} > 1$) can be given as follows:

$$\frac{\partial s}{\partial t} = \frac{\partial(e_a/e_s)}{\partial t} = \frac{1}{e_s} \frac{\partial e_a}{\partial t} - \frac{e_a}{e_s^2} \frac{\partial e_s}{\partial t} = \frac{1}{e_s} \frac{\partial e_a}{\partial t} - \frac{e_a}{e_s^2} \frac{\partial e_s}{\partial T} \frac{\partial T}{\partial t}. \quad (1)$$

Using the Clausius–Clapeyron-equation (Götz & Rákóczi, 1981) $\left(\frac{\partial e_s}{\partial T} \cong \frac{de_s}{dT} = \frac{L_{lv}e_s}{R_v T^2}\right)$ we get

$$\frac{\partial s}{\partial t} = \frac{1}{e_s} \frac{\partial e_a}{\partial t} - \frac{e_a}{e_s^2} \frac{L_{lv}e_s}{R_v T^2} \frac{\partial T}{\partial t} \quad (2)$$

where the L_{lv} is the latent heat of vaporization for water ($L_{lv} \cong 2.5 \cdot 10^6 \text{ J kg}^{-1}$, R_v is the specific gas constant for the water vapour ($R_v = 461 \text{ J kg}^{-1} \text{ K}^{-1}$). Because the saturation vapor pressure (e_s) is a function of only the single independent variable T , the partial and total derivatives are equivalent in this case (Lawrence, 2005).

Eq. (2) can also be written with specific humidity,

$$\frac{\partial s}{\partial t} = \frac{\partial(q_a/q_s)}{\partial t} = \frac{1}{q_s} \frac{\partial q_a}{\partial t} - \frac{q_a}{q_s^2} \frac{L_{lv}q_s}{R_v T^2} \frac{\partial T}{\partial t}, \quad (3)$$

where $q_a = \frac{\rho_a}{\rho_m}$, $q_s = \frac{\rho_s}{\rho_m}$ is the supersaturated and saturated specific humidity, and ρ_a , ρ_s , ρ_m is the density of supersaturated and saturated water vapor, and the moist air, respectively. We assume that $\rho_m = \text{const.}$

The local temporal derivate of temperature $\left(\frac{\partial T}{\partial t}\right)$ is divided into two parts as advection and non-advection parts.

$$\frac{\partial T}{\partial t} = \frac{\partial T}{\partial t}\Big|_{adv.} + \frac{\partial T}{\partial t}\Big|_{nonadv.}. \quad (4)$$

The advection depends on the horizontal temperature gradient ($\nabla_h T$) and the wind speed (\mathbf{v}_h):

$$\frac{\partial T}{\partial t}\Big|_{adv.} = -\mathbf{v}_h \cdot \nabla_h T. \quad (5)$$

The non-advection term consists of the convection, $-\mathbf{w} \frac{\partial T}{\partial z}$, and the nonadiabatic processes as the condensation, $-\frac{L_{lv}}{c_{pm}} \frac{dq_a}{dt}$, where c_{pm} is the heat capacity of the moist air with constant pressure. The convection is negligible compared with the condensation because the latent heat released during condensation dominates over sensible heat fluxes due to convection (Schumacher, 2004).

$$\frac{\partial T}{\partial t} \cong \frac{\partial T}{\partial t}\Big|_{adv.} - \frac{L_{lv}}{c_{pm}} \frac{dq_a}{dt}. \quad (6)$$

In this case, we also assume negligible convection,

$$\frac{\partial q_a}{\partial t} = \left. \frac{\partial q_a}{\partial t} \right|_{adv.} + \frac{dq_a}{dt}, \quad (7)$$

The reason of the change of the supersaturation can be divided into two parts, caused due to advection and condensation:

$$\frac{\partial s}{\partial t} = \frac{\partial(q_a/q_s)}{\partial t} = - \left. \frac{q_a L_{lv} q_s}{q_s^2 R_v T^2} \frac{\partial T}{\partial t} \right|_{adv.} + \left. \frac{1}{q_s} \frac{\partial q_a}{\partial t} \right|_{adv.} + \left. \frac{1}{q_s} \frac{\partial q_a}{\partial t} \right|_{cond.} + \left. \frac{q_a L_{lv}}{q_s R_v T^2} \frac{L_{lv}}{c_{pm}} \frac{\partial q_a}{\partial t} \right|_{cond.}, \quad (8)$$

$$\frac{\partial s}{\partial t} = \left(1 + \frac{q_a L_{lv}^2}{c_{pm} R_v T^2} \right) \left. \frac{1}{q_s} \frac{\partial q_a}{\partial t} \right|_{cond.} - \left. \frac{q_a L_{lv}}{q_s R_v T^2} \frac{\partial T}{\partial t} \right|_{adv.} + \left. \frac{1}{q_s} \frac{\partial q_a}{\partial t} \right|_{adv.} \quad (9)$$

Eq. (9) is useful to evaluate the rate of supersaturation. The rate of supersaturation is a prognostic variable in many numerical models to evaluate the activation of the hygroscopic aerosol particles. The importance of local change of temperature and specific humidity is presented to evaluate the change of supersaturation ratio. In the current study the results of cooling rate are presented. Quantification of the effects responsible for the development of the cooling rate is not the purpose of the research. Similar methodology for change point detection of specific humidity time series can be also used, but the results are not presented here (our measurement system is not gives the opportunity to direct investigation of supersaturation).

Window based change point detection method

To analyse the cooling rate, we analysed the 10 s as well as 10 Hz time resolution temperature time series observed by the temperature sensors installed on the 30 m tower and from the sonic temperature, respectively. The temperature time series have been sampled 3–4 hours before the beginning of foggy event and divided into segments based on the breakpoints detected in the time series. Breakpoint detection was used because temperature decrease is not monotonous throughout this 3–4 hours' time window. Cooling rate is equal to the slope of linear regression fitted to the time series of temperature. The breakpoints are identified using the ‘‘Window-based change point detection method’’ (Ahmed et al., 2008; Li et al., 2010; Matyasovszky & Ljungqvist, 2012; Truong et al., 2020).

Window-based change point detection method is a non-parametric CUSUM (*Cumulative Sum Control Chart*) algorithm to detect abrupt changes in the time evolution of the data. This algorithm uses two sliding windows on the data series and statistical properties of the data series within these two windows are compared with a discrepancy measure (Ahmed et al., 2008; Li et al., 2010; Truong et al., 2020). If a discrepancy exists between the two data series inside the two sliding windows, then a peak is observed. Once the discrepancy finding procedure is completed, a peak finding processes is started to detect the breakpoints in the data series. The discrepancy can be calculated using the Student's *t*-test or respective cost functions, which are present in the ruptures python library [1 – ruptures]. The discrepancy between the two sub-signals (data series) for a cost function $c(\cdot)$ divided for each sliding window is given as:

$$(y_{a,t}, y_{t,b}) = c(y_{a,b}) - c(y_{a,t}) - c(y_{t,b}) \quad (1 \leq a < t < b \leq T), \quad (10)$$

where $\{y_t\}_{t=1}^T$ is the input signal, and $a < t < b$ are the indices. The cost functions are used to test the homogeneity of the time series/signal. If the sub-signals (fragments) in a time series/signal are homogeneous, then the discrepancy of the cost function is lower, otherwise if the sub-signals are not homogeneous, then the discrepancy calculated in the cost functions are higher. The sliding windows a, \dots, t and t, \dots, b fall in the same segment if the statistical

properties (discrepancy) calculated using the cost function are the same. If the discrepancy calculated using the cost function is not the same or significantly higher, then these two segments are not similar to each other.

The algorithm has a low time complexity and can detect single or multiple breakpoints in a data series. This method can be applied also if the number of change points or breakpoints in a data series is not known beforehand (Truong et al., 2020). The performance is improved as this algorithm removes the effect of data points related to the last detected breakpoints, and thus only normal data points are kept in a sliding window at a given time (Truong et al., 2020).

The python package Ruptures [1 – ruptures] has been utilized for employing the Window-based change point detection method, and each temperature time series has been analysed using two cost function namely CostL2 and CostRbf. CostL2 function also known as the Least squared deviation, is a function that detects mean-shifts in a signal or timeseries (Truong et al., 2020). On the other hand, CostRbf function also known as the Kernelized mean change, is able to detect the changes in the probability distribution of a random variable. It is a non-parametric method and can be used for a wide variety of tasks of change point detection (Truong et al., 2020).

In the CostL2 or the mean shift model, the distribution of the variable is assumed to be Gaussian with fixed variance. This cost function is also mentioned in the literature as quadratic error loss and is given as follows:

$$C_{L2}(y_{a..b}) := \sum_{t=a+1}^b \|y_t - \bar{y}_{a..b}\|_2^2, \quad (11)$$

where $\bar{y}_{a..b}$ is the empirical mean of the signal $y_{a..b}$.

CostRbf is a Kernel-based change point detection cost function. Kernel-based methods can detect breakpoints in a non-parametric setting (Celisse et al., 2018; Truong et al., 2020). The original signal/timeseries is mapped on to a reproducing Hilbert space \mathcal{H} . The Hilbert space is associated with a user defined kernel $k(.,.): \mathbb{R}^d \times \mathbb{R}^d \rightarrow \mathbb{R}$. The mapping function, which maps the signal/timeseries on the Hilbert space is defined as $\phi: \mathbb{R}^d \rightarrow \mathcal{H}$. $\phi: \mathbb{R}^d \rightarrow \mathcal{H}$ is also known as a canonical feature map and it is defined as $\phi(y_t) = k(y_t, .) \in \mathcal{H}$. The inner products and norm on \mathcal{H} for a kernel k can be defined as:

$$\langle \phi(y_s) | \phi(y_t) \rangle_{\mathcal{H}} = k(y_s, y_t) \quad (12)$$

$$\|\phi(y_t)\|_{\mathcal{H}}^2 = k(y_t, y_t) \quad (13)$$

For a given kernel $k(.,.): \mathbb{R}^d \times \mathbb{R}^d \rightarrow \mathbb{R}$, the associated cost function can be calculated as follows:

$$c_{kernel}(y_{a..b}) := \sum_{t=a+1}^b \|\phi(y_t) - \bar{\mu}_{a..b}\|_{\mathcal{H}}^2 \quad (14)$$

where, $\{\phi(y_t)\}_{t=a+1}^b$ is the embedded/transformed signal in the Hilbert space and $\bar{\mu}_{a..b}$ is the empirical mean of the embedded signal. The cost function is able to detect the mean shifts in the signal as it is assumed that under certain conditions of the kernel functions, the changes in mean shifts coincide with the changes in probability distribution (Celisse et al., 2018; Truong et al., 2020). Any inner product in \mathcal{H} can be translated in terms of the kernel k by using a kernel trick, by using the Eqs. 12 and 13 (Celisse et al., 2018). The cost function defined in the Eq. (14) can be written in simpler form after performing the kernel trick. For any samples $y_s, y_t \in \mathbb{R}^d$, the kernelized cost function is defined as:

$$c_{kernel}(y_{a..b}) := \sum_{t=a+1}^b k(y_t, y_t) - \frac{1}{b-a} \sum_{s,t=a+1}^b k(y_s, y_t) \quad (15)$$

In this paper, the CostRbf function is an example of using a cost function based on Gaussian kernel. The CostRbf function is then defined as:

$$C_{rbf}(y_{a..b}) := (b - a) - \frac{1}{b-a} \sum_{s,t=a+1}^b \exp(-\gamma \|y_s - y_t\|^2), \quad (16)$$

where $\gamma > 0$, is the bandwidth parameter.

The advantage of using kernels is that they can be used on any data type, and the only precondition is that we should be able to define the kernel on that data.

Breakpoint detection and cooling rate

Breakpoints detected in temperature data at 9 m, 23 m and 30 m heights

The foggy event occurring in the time period of 3:30–22:30 UTC on 24th November in 2020 was chosen to evaluate the cooling rate prior to the formation of the fog. Data observed in the time period of 00:00–04:30 UTC was analysed to calculate the cooling rate. Fog onset was detected by ceilometer (LUFFT CHM 15k) at 03:30 UTC.

Figure 2 (a-b) reveals that multiple breakpoints have been detected using the window-based change point detection method. The breakpoints of time series of temperature observed at height of 9 m are denoted by red dashed lines and the corresponding timestamps are summarized in *Table 2*. The CostL2 function and CostRbf function used inside the window-based search method, detected 9 and 8 breakpoints, respectively. The first 8 breakpoints detected by the two cost functions are almost at the same timestamp with a small difference of only 2–3 minutes except for the 5th breakpoint where the time difference of 14 minutes can be found.

Red, vertical dashed lines in *Figure 2 (c-d)* detect breakpoints for temperature observed at the height of 23 m. Both CostL2 and CostRbf functions used inside the window-based search method detect 5 points. The timestamps of the detected breakpoints are shown in *Table 2*. It can be seen from *Table 2* that the 1st breakpoint detected by both the cost functions is at exactly same time, whereas the largest difference of 18 minutes is observed in the case of the 3rd breakpoint. Such differences can be attributed to the fact that CostL2 function detects breakpoints on the basis of changes in mean, whereas CostRbf detects changes based on changes in probability distribution of the data series.

Figure 2 (e-f) shows the breakpoints detected in the case of temperature data observed by sonic anemometer. Both cost functions detected 5 breakpoints. The two methods detect the 2nd, 3rd and the 5th breakpoints at exactly the same time, while the remaining breakpoints were detected with a time differences of 10–20 s.

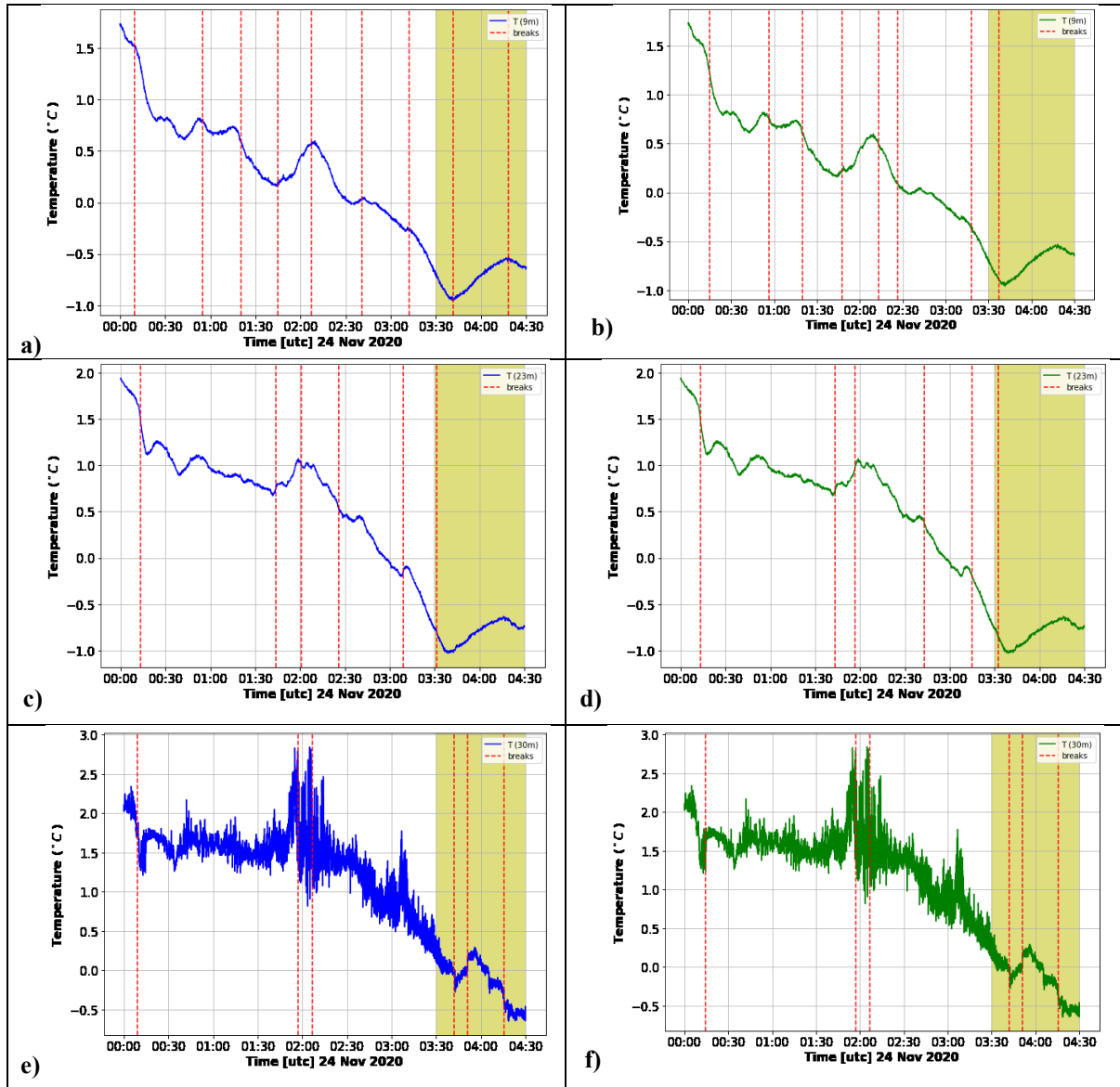


Figure 2: Temperature time series, sampled from 00:00 UTC to 04:30 UTC on 24th November, 2020.

Detected breakpoints are denoted by vertical dashed red lines. Panel a) and b) denote the detected breakpoints for temperature observed at the height of 9 m, evaluated by detection methods of CostL2 and CostRbf, respectively. Panel c) and d) denote the detected breakpoints for temperature observed at the height of 23 m, evaluated by detection methods of CostL2 and CostRbf, respectively. Panel e) and f) denote the detected breakpoints for sonic temperature (Mauder and Foken, 2015) observed by sonic anemometer at the height of 30 m, evaluated by methods of CostL2 and CostRbf, respectively. ([e-f] is corrected sonic temperature time series.) The sonic temperature was corrected based on the extrapolated main virtual temperature profile using the measurement in 9 m and 23 m. The sonic temperature was adjusted by -10.15 °C (using the mean virtual temperature at 30 m height for the measurement period). The time variation of sonic temperature is real, but the measured (original) values are slightly (more than 3.6% (in K)) overestimated. The deviation of raw values from real sonic (near virtual) temperature is due to the difference between the distances of the three pairs of sensors from sonic anemometer and the distance is set in the factory software for calculating temperature.

Table 2: Timestamps of breakpoints detected using CostL2 and Cost Rbf cost functions within the window-based break point detection method in the temperature time series observed by sensors at 9 m, 23 m and 30 m. (Temperature time series, sampled from 00:00 UTC to 04:30 UTC on 24th November, 2020.)

S. No.	T9m_L2 [timestamp - UTC]	T9m_Rbf [timestamp - UTC]	T23m_L2 [timestamp - UTC]	T23_Rbf [timestamp - UTC]	T30_L2 [timestamp - UTC]	T30_Rbf [timestamp - UTC]
1	2020-11-24 00:09:50	2020-11-24 00:14:50	2020-11-24 00:13:10	2020-11-24 00:13:10	2020-11-24 00:08:59	2020-11-24 00:09:09
2	2020-11-24 00:54:50	2020-11-24 00:56:30	2020-11-24 01:44:00	2020-11-24 01:43:10	2020-11-24 01:56:59	2020-11-24 01:56:59
3	2020-11-24 01:20:40	2020-11-24 01:19:50	2020-11-24 02:00:40	2020-11-24 01:56:30	2020-11-24 02:06:44	2020-11-24 02:06:39
4	2020-11-24 01:44:50	2020-11-24 01:47:20	2020-11-24 02:25:40	2020-11-24 02:43:10	2020-11-24 03:41:49	2020-11-24 03:41:49
5	2020-11-24 02:07:20	2020-11-24 02:13:10	2020-11-24 03:09:00	2020-11-24 03:14:50	2020-11-24 03:51:04	2020-11-24 03:51:09
6	2020-11-24 02:40:40	2020-11-24 02:26:30	2020-11-24 03:31:30	2020-11-24 03:32:20	2020-11-24 04:15:19	2020-11-24 04:15:19
7	2020-11-24 03:12:20	2020-11-24 03:18:10				
8	2020-11-24 03:41:30	2020-11-24 03:37:20				
9	2020-11-24 04:18:10					

Evaluation of cooling rate based on breakpoints detection

The cooling rates were evaluated by using the detected breakpoints. Using linear regression, a line was fitted to each sector of the time series bounded by two breakpoints. Linear regression was performed over the sectors time series after 02:00 UTC, because the temperature started to decrease clearly after 02:00 UTC. *Table 3* summarizes the slope and intercept parameters of lines that were fitted over 3 sectors of the time series of temperature observed at the height of 9 m and 23 m (*Figure 2(a-d)*). In the case of sonic temperature data, the linear fitting was performed for only one sector of time series, because breakpoints were not detected by neither of the cost functions in the time interval of 02:00–03:30 UTC (before the fog onset).

At both altitudes (9 m and 23 m) the sum of the sectors of the time series fragment is 20–40 minutes long. For the temperature measurements done at 9 m and 23 m height, and using CostL2 function for detecting breakpoints, we found that the cooling rate was the largest in the third sector (which started 20–30 minutes before fog onset). The cooling rates were $0.026 \text{ }^\circ\text{C min}^{-1}$ ($1.56 \text{ }^\circ\text{C hr}^{-1}$) and $0.035 \text{ }^\circ\text{C min}^{-1}$ ($2.1 \text{ }^\circ\text{C hr}^{-1}$), respectively. The lowest cooling rates of $0.011 \text{ }^\circ\text{C min}^{-1}$ ($0.66 \text{ }^\circ\text{C hr}^{-1}$) and $0.018 \text{ }^\circ\text{C min}^{-1}$ ($1.08 \text{ }^\circ\text{C hr}^{-1}$) were found in the second sectors. The average cooling rates evaluated by CostL2 (calculated as the average of all the three sectors) at the altitudes of 9 m and 23 m were $0.019 \text{ }^\circ\text{C min}^{-1}$ ($1.14 \text{ }^\circ\text{C hr}^{-1}$) and $0.023 \text{ }^\circ\text{C min}^{-1}$ ($1.38 \text{ }^\circ\text{C hr}^{-1}$), respectively.

Using the CostRbf function the largest and smallest cooling rates of $0.037 \text{ }^\circ\text{C min}^{-1}$ ($2.22 \text{ }^\circ\text{C hr}^{-1}$) and $0.017 \text{ }^\circ\text{C min}^{-1}$ ($1.02 \text{ }^\circ\text{C hr}^{-1}$) can be found in the third and the first sector of temperature time series observed at the altitude of 23 m, respectively. In the case of time series observed at the height of 9 m, the largest cooling rate of $0.033 \text{ }^\circ\text{C min}^{-1}$ ($1.98 \text{ }^\circ\text{C hr}^{-1}$) was observed in the first sector, which started 1.5 hours before the fog onset, followed by the third ($0.028 \text{ }^\circ\text{C min}^{-1}$ ($1.68 \text{ }^\circ\text{C hr}^{-1}$)) and the second sector ($0.008 \text{ }^\circ\text{C min}^{-1}$ ($0.48 \text{ }^\circ\text{C hr}^{-1}$)), respectively. For the sonic temperature data, since no breakpoints are detected between 02:00 UTC and 03:30 UTC, we get a single sector of the time series. The evaluated cooling rates using the two different functions were the same at $0.017 \text{ }^\circ\text{C min}^{-1}$ ($1.02 \text{ }^\circ\text{C hr}^{-1}$).

Using CostRbf function the average cooling rate for the altitudes of 9 m and 23 m are $0.024 \text{ } ^\circ\text{C min}^{-1}$ ($1.44 \text{ } ^\circ\text{C hr}^{-1}$) and $0.023 \text{ } ^\circ\text{C min}^{-1}$ ($1.38 \text{ } ^\circ\text{C hr}^{-1}$), respectively.

Table 3: Slope ($^\circ\text{C min}^{-1}$) and intercept ($^\circ\text{C}$) parameters evaluated by linear regression method for each sector of time series of temperature observed at the heights of 9 m and 23 m, furthermore for that of sonic temperature observed at the height of 30 m.

S.No.		T9m_L2		T9m_Rbf		
	Time series sector [UTC]	Slope ($^\circ\text{C min}^{-1}$)	Intercept ($^\circ\text{C}$)	Time series fragment [UTC]	Slope ($^\circ\text{C min}^{-1}$)	Intercept ($^\circ\text{C}$)
1	2020-11-24 02:07:20 - 2020-11-24 02:40:40	-0.021	0.581	2020-11-24 02:13:10 - 2020-11-24 02:26:30	-0.033	0.511
2	2020-11-24 02:40:40 - 2020-11-24 03:12:20	-0.011	0.074	2020-11-24 02:26:30 - 2020-11-24 03:18:10	-0.008	0.113
3	2020-11-24 03:12:20 - 2020-11-24 03:41:30	-0.026	-0.222	2020-11-24 03:18:10 - 2020-11-24 03:37:20	-0.028	-0.363
S.No.		T23m_L2		T23m_Rbf		
	Time series sector [UTC]	Slope ($^\circ\text{C min}^{-1}$)	Intercept ($^\circ\text{C}$)	Time series fragment [UTC]	Slope ($^\circ\text{C min}^{-1}$)	Intercept ($^\circ\text{C}$)
1	2020-11-24 02:00:40 - 2020-11-24 02:25:40	-0.018	1.081	2020-11-24 01:56:30 - 2020-11-24 02:43:10	-0.017	1.11
2	2020-11-24 02:25:40 - 2020-11-24 03:09:00	-0.018	0.59	2020-11-24 02:43:10 - 2020-11-24 03:14:50	-0.016	0.261
3	2020-11-24 03:09:00 - 2020-11-24 03:31:30	-0.035	-0.01	2020-11-24 03:14:50 - 2020-11-24 03:32:20	-0.037	-0.201
S.No.		T30m_L2		T30m_Rbf		
	Time series sector [UTC]	Slope* ($^\circ\text{C min}^{-1}$)	Intercept* ($^\circ\text{C}$)	Time series fragment [UTC]	Slope* ($^\circ\text{C min}^{-1}$)	Intercept* ($^\circ\text{C}$)
1	2020-11-24 02:06:44 - 2020-11-24 03:41:49	-0.017	1.74	2020-11-24 02:06:39 - 2020-11-24 03:41:49	-0.017	1.74

*Slope and intercept from the corrected sonic temperature time series.

Conclusions

The Budapest fog experiment was carried out during the winter of 2020–21 (Nov 2020–April 2021) at the observatory of the HMS located at the *edge of* Budapest (station ID 12843).

We utilized the temperature time series with a time resolution of 10 s and 10 Hz coming from the temperature sensors implemented at the altitudes of 9 m, 23 m, and raw sonic temperature from sonic anemometer implemented at a height of 30 m (on top of the tower, with preliminary correction) for calculating the cooling rate. The fog event that occurred on November 24 (03:30–22:30 UTC), 2020 was chosen to evaluate and analyze the cooling rate. Cooling near the surface layer is an important precursor for fog formation and cooling of the surface layer coupled with increase of relative humidity near the saturation allows the formation of water droplets by condensation resulting in onset of fog. Window based search algorithm present in the python ruptures library [1 – ruptures] was utilised to analyze the breakpoints in the temperature time series prior to the calculation of cooling rate. The breakpoints were detected using both the CostL2 and CostRbf functions. Time series of temperature observed after 02:00 UTC at the altitudes of 9 m, 23 m and 30 m were chosen to perform linear regression analysis.

In case of data observed at the altitudes of 9 m and 23 m, three sectors, each of them roughly 20–40 minutes long, were detected. The cooling rate was defined as the slope of the fitted linear equation. When CostL2 was used, the cooling rate was found to be the highest in the third sectors. The third sectors started 30–40 minutes before the fog onset and cooling rates in the third sectors at the altitudes of 9 m and 23 m were $0.026 \text{ } ^\circ\text{C min}^{-1}$ ($1.56 \text{ } ^\circ\text{C hr}^{-1}$) and $0.035 \text{ } ^\circ\text{C min}^{-1}$ ($2.1 \text{ } ^\circ\text{C hr}^{-1}$), respectively. However, when using CostRbf function, the cooling

rate was the highest only in the third sector of data series observed at the altitude of 23 m, whereas in the case of temperature observed at 9 m the largest cooling rate was evaluated in the first sector.

The average cooling rate (calculated as the average of all the three sectors) for 9 m temperature and 23 m temperature time series using CostL2 is $0.019\text{ }^{\circ}\text{C min}^{-1}$ ($1.14\text{ }^{\circ}\text{C hr}^{-1}$) and $0.023\text{ }^{\circ}\text{C min}^{-1}$ ($1.38\text{ }^{\circ}\text{C hr}^{-1}$), respectively. Whereas, when using CostRbf function, the average cooling rate were $0.024\text{ }^{\circ}\text{C min}^{-1}$ ($1.44\text{ }^{\circ}\text{C hr}^{-1}$) and $0.023\text{ }^{\circ}\text{C min}^{-1}$ ($1.38\text{ }^{\circ}\text{C hr}^{-1}$), respectively, for 9 m and 23 m temperature.

Assembling the cooling rates evaluated by the CostL2 and CostRbf functions, we can say that the cooling rate at the altitude of 9 m is in the range of $1.14\text{ }^{\circ}\text{C hr}^{-1}$ – $1.44\text{ }^{\circ}\text{C hr}^{-1}$ and at the altitude of 23 m it is $1.38\text{ }^{\circ}\text{C hr}^{-1}$. We observe that with increase in height, the cooling rates, calculated by both Cost functions at 23 m, are the same whereas there is a larger difference at 9 m height. Such differences can arrive due to the method in which both the cost functions detect breakpoints. CostRbf function (based on Gaussian kernel) essentially detects changes in the probability distribution of a random variable whereas Cost L2 detect mean shifts in a time series. This led to breakpoints getting detected at different timestamps causing difference in length of time series fragments. We can see from *Table 3* that the length of the first sector in the case of temperature time series at 9 m is different as CostRbf function detected the breakpoint earlier than CostL2.

In the case of corrected sonic temperature (using the reference extrapolated virtual temperature for 30 m level) time series, 6 breakpoints were detected by both the CostL2 and CostRbf functions. Since there were no breakpoints detected by both cost functions between 02:00 UTC until the fog onset, only one cooling rate was evaluated by both cost functions with the same average value of $0.017\text{ }^{\circ}\text{C min}^{-1}$ ($1.02\text{ }^{\circ}\text{C hr}^{-1}$). Price (2011) and Price et al. (2018) calculated the cooling rates for different locations with different topography. They found lower cooling rates in evening in wider and open valleys as compared to narrow and deep valleys due to the decoupling of narrow and deep valleys with the overlying flow. However, fogs appeared more in wide and open valleys as they were able to cool for longer time period and transformed into the coldest sites. The wide and open valleys cooled slowly at a rate of approximately $1\text{ }^{\circ}\text{C hr}^{-1}$ whereas narrower valleys cooled at $1.5\text{ }^{\circ}\text{C hr}^{-1}$.

The calculation of cooling rate is significant in the sense that it can be used in the calculation of rate of change in supersaturation, which in turn is an appropriate prognostic variable in the microphysics schemes implemented in weather prediction models. We plan to investigate the rate of change in relative humidity and saturation prior to fog occurrence to better understand the fine structure of the fog evolution.

Funding: The measurement campaign was performed in the frame of GINOP2.3.2-15-2016-00007, GINOP-2.3.2-15-2016-00055, OTKA-138176 and CA20108 - FAIR Network of micrometeorological measurements (FAIRNESS) COST Action. The experiment is connected with the PANNEX program which is part of the Regional Hydroclimate Project (RHP) of the World Climate Research Programme (WCRP).

References

- Ahmed, E., Clark, A., Mohay, G., 2008: A novel sliding window based change detection algorithm for asymmetric traffic. In *2008 IFIP International Conference on Network and Parallel Computing*, 168–175. IEEE. <https://doi.org/10.1109/NPC.2008.81>
- Celisse, A., Marot, G., Pierre-Jean, M., Rigail, G. J., 2018: New efficient algorithms for multiple change-point detection with reproducing kernels. *Computational Statistics and Data Analysis*, 128(C): 200–220. <https://doi.org/10.1016/j.csda.2018.07.002>

- Dupont, J.C., Haeffelin, M., Stolaki, S., Elias, T., 2016: Analysis of dynamical and thermal processes driving fog and quasi-fog life cycles using the 2010–2013 ParisFog dataset. *Pure and Applied Geophysics*, 173(4): 1337–1358. <https://doi.org/10.1007/s00024-015-1159-x>
- Duynkerke, P.G., 1999: Turbulence, radiation and fog in Dutch stable boundary layers. *Boundary-Layer Meteorology*, 90(3): 447–477. <https://doi.org/10.1023/A:1026441904734>
- Elliott, W.P., 1964: The height variation of vertical heat flux near the ground. *Quaternaly Journal of the Royal Meteorological Society*, 90(385): 260–265. <https://doi.org/10.1002/qj.49709038504>
- Funk, J.P., 1960: Measured radiative flux divergence near the ground at night. *Quaternaly Journal of the Royal Meteorological Society*, 86(369): 382–389. <https://doi.org/10.1002/qj.49708636910>
- Götz, G., Rákóczi, F., 1981: *Fundamentals of Dynamic Meteorology* (A dinamikus meteorológia alapjai), Tankönyvkiadó, Budapest, 483 p. ISBN 963 17 5580 0 (In Hung.)
- Haeffelin, M., Bergot, T., Elias, T., Tardif, R., Carrer, D., Chazette, P., Colomb, M., Drobinski, P., Dupont, E., Dupont, J.C., Gomes, L., 2010: ParisFog: Shedding new light on fog physical processes. *Bulletin of the American Meteorological Society*, 91(6): 767–783. <https://doi.org/10.1175/2009BAMS2671.1>
- Haeffelin, M., Dupont, J.C., Boyouk, N., Baumgardner, D., Gomes, L., Roberts, G., Elias, T., 2013: A comparative study of radiation fog and quasi-fog formation processes during the ParisFog field experiment 2007. *Pure and Applied Geophysics*, 170(12): 2283–2303. <https://doi.org/10.1007/s00024-013-0672-z>
- Lawrence, M.G., 2005: The relationship between relative humidity and the dewpoint temperature in moist air: A simple conversion and applications. *Bulletin of the American Meteorological Society*, 86(2): 225–234. <https://doi.org/10.1175/BAMS-86-2-225>
- Li, W., Guo, W., Luo, X., Li, X., 2010: On sliding window based change point detection for hybrid SIP DoS attack. In *2010 IEEE Asia-Pacific Services Computing Conference*, 425–432. IEEE. <https://doi.org/10.1109/APSCC.2010.84>
- Lin, D., Katurji, M., Revell, L. E., Khan, B., Osborne, N., Soltanzadeh, I., Kremser, S., 2022: Fog type classification using a modified Richardson number for Christchurch, New Zealand. *International Journal of Climatology*, 43(1): 314–330. <https://doi.org/10.1002/joc.7761>
- Mason, J., 1982: The physics of radiation fog. *Journal of the Meteorological Society of Japan. Ser. II*, 60(1): 486–499. https://doi.org/10.2151/jmsj1965.60.1_486
- Matyasovszky, I., Ljungqvist, F.C., 2012: Abrupt temperature changes during the last 1,500 years. *Theoretical and Applied Climatology*, 112: 215–225. <https://doi.org/10.1007/s00704-012-0725-8>
- Price, J., 2011: Radiation Fog. Part I: Observations of Stability and Drop Size Distributions. *Boundary-Layer Meteorology*, 139: 167–191. <https://doi.org/10.1007/s10546-010-9580-2>
- Price, J.D., Lane, S., Boutle, I.A., Smith, D.K.E., Bergot, T., Lac, C., Duconge, L., McGregor, J., Kerr-Munslow, A., Pickering, M., Clark, R., 2018: LANFEX: a field and modeling study to improve our understanding and forecasting of radiation fog. *Bulletin of the American Meteorological Society*, 99(10): 2061–2077. <https://doi.org/10.1175/BAMS-D-16-0299.1>
- Rangognio, J., Tulet, P., Bergot, T., Gomes, L., Thouron, O., Leriche, M., 2009: Influence of aerosols on the formation and development of radiation fog. *Atmospheric Chemistry and Physics Discussions*, 9(5): 17963–18019. <https://doi.org/10.5194/acpd-9-17963-2009>
- Rider, N.E., Robinson, G.D., 1951: A study of the transfer of heat and water vapour above a surface of short grass. *Quaternaly Journal of the Royal Meteorological Society*, 77(333): 375–401. <https://doi.org/10.1002/qj.49707733305>

- Schumacher, C., Houze, R.A. Kraucunas, I., 2004. The tropical dynamical response to latent heating estimates derived from the TRMM precipitation radar. *Journal of Atmospheric Sciences*, 61(12): 1341–1358. [https://doi.org/10.1175/1520-0469\(2004\)061<1341:TTDRTL>2.0.CO;2](https://doi.org/10.1175/1520-0469(2004)061<1341:TTDRTL>2.0.CO;2)
- Tardif, R., Rasmussen, R.M., 2007: Event-based climatology and typology of fog in the New York City region. *Journal of Applied Meteorology and Climatology*, 46(8): 1141–1168. <https://doi.org/10.1175/JAM2516.1>
- Truong, C., Oudre, L., Vayatis, N., 2020: Selective review of offline change point detection methods. *Signal Processing*, 167p. 107299. <https://doi.org/10.1016/j.sigpro.2019.107299>
- Weidinger, T., Gyöngyösi, A.Z., Arun, G., Tordai, Á., Krámer, T., Torma, P., Reháč, A., Szilágyi, M., Horváth, Á., Horváth, Gy., Bottyán, Zs., Cséplő, A., Lázár, I., Imre, K., Kardos, P., Geresdi, I., 2021: Micrometeorological fog experiments in Budapest and in Sió Valley near Lake Balaton (2018-2021). *EMS Annual Meeting Abstracts*, 18, EMS2021-304. <https://doi.org/10.5194/ems2021-304>

Online references

[1 – ruptures] <https://centre-borelli.github.io/ruptures-docs/>

ORCID

- I. Geresdi  <https://orcid.org/0000-0002-3160-7900>
- Á.V. Tordai  <https://orcid.org/0000-0002-8617-0531>
- P. Torma  <https://orcid.org/0000-0001-9282-6931>
- Z. Ferenczi  <https://orcid.org/0000-0002-9163-4628>
- T. Weidinger  <https://orcid.org/0000-0001-7500-6579>